



Shortwave Array Spectroradiometer-Hemispheric (SAS-He): Design and Evaluation

Evgueni Kassianov¹, Connor J. Flynn², James C. Barnard³, Brian D. Ermold¹, Jennifer M. Comstock¹

¹Pacific Northwest National Laboratory, Richland, WA, USA

5 ²School of Meteorology, University of Oklahoma, Norman, OK, USA

³University of Nevada, Reno, NV, USA

Correspondence to: Evgueni Kassianov (Evgueni.Kassianov@pnnl.gov)

Abstract. A novel ground-based radiometer, referred to as the Shortwave Array Spectroradiometer-Hemispheric (SAS-He), is introduced. This radiometer uses the shadow band technique to report total irradiance and its direct and diffuse components frequently (every 30 sec) with continuous spectral coverage (350-1700 nm) and moderate spectral (~2.5 nm ultraviolet/visible, and ~6 nm shortwave-infrared) resolution. The SAS-He's performance is evaluated using integrated datasets collected over coastal regions during three field campaigns supported by the U.S. Department of Energy's (DOE's) Atmospheric Radiation Measurement (ARM) Program, namely (1) Two-Column Aerosol Project (TCAP; Cape Cod, Massachusetts), (2) Tracking Aerosol Convection Interactions Experiment (TRACER; in and around Houston, Texas), and (3) Eastern Pacific Cloud Aerosol Precipitation Experiment (EPCAPE; La Jolla, California). We compare (i) aerosol optical depth (*AOD*) and total optical depth (*TOD*) derived from the direct irradiance, (ii) the diffuse irradiance and direct-to-diffuse ratio (*DDR*) calculated from two components of the total irradiance. As part of the evaluation, both *AOD* and *TOD* derived from the SAS-He direct irradiance are compared to those provided by collocated Cimel sunphotometer (CSPHOT) at five (380, 440, 500, 675, 870 nm) and two (1020, 1640 nm) wavelengths, respectively. Additionally, the SAS-He diffuse irradiance and *DDR* are contrasted with their counterparts offered by a collocated Multi-Filter Rotating Shadowband Radiometer (MFRSR) at six (415, 500, 615, 675, 870, 1625 nm) wavelengths. Overall, reasonable agreement is demonstrated between the compared products despite the challenging observational conditions associated with varying aerosol loadings and diverse types of aerosols and clouds. The *AOD*- and *TOD*-related values of root-mean-square error are within the expected measurement uncertainty of *AOD* (0.01-0.02).

1 Introduction

Clouds and atmospheric aerosols are important drivers of the Earth radiation budget (Voigt et al., 2021; Li et al., 2022). They have unique fingerprints across a wide spectral range, which includes ultraviolet (UV), visible (VIS), near-infrared (NIR) and shortwave-infrared (SWIR) spectral bands. Moreover, cloud droplets and aerosol particles with a wide range of sizes and shapes modify distinctly the angular distribution of the scattered solar radiation (Hansen and Travis, 1974; Kokhanovsky,



2004; Yang et al., 2013). Thus, advanced cloud and aerosol retrievals over different surface types involve both multi-spectral and multi-angular measurements from surface, air, and space (Chen et al., 2022; Puthukkudy et al., 2020; Matar et al., 2023; Michalsky and Kiedron, 2022). To illustrate, the aircraft-based sensor named Spectrometer for Sky-Scanning, Sun-Tracking Atmospheric Research (4STAR; wavelength range: 350–1650 nm) with sky-scanning and hyperspectral abilities has offered
35 valuable information on above-cloud aerosol optical depth (*AOD*) (LeBlanc et al., 2020), while solar irradiances measured by aircraft-based Solar Spectral Flux Radiometer (SSFR; wavelength range: 350–2100 nm) have been used to provide spectral surface albedo (Coddington et al., 2008) and cloud spectral absorption (Kindel et al., 2011), which is a function of cloud optical thickness and droplet effective radius. The combined 4STAR and SSFR airborne measurements have been utilized to derive heating rate profiles over a climate-important region (Cochrane et al., 2022).

40 Airborne measurements can infer valuable properties of clouds and aerosols with high temporal resolution. However, these episodic measurements represent a relatively short period (e.g., several weeks) and a given location (LeBlanc et al., 2020; Cochrane et al., 2022). Conversely, satellite observations have been used successfully to extract a wealth of information about clouds and aerosols near-globally (Platnick et al., 2017; Gumber et al., 2023). Nevertheless, these observations occur infrequently (typically several times a day) and do not capture the diurnal cycle. The airborne and satellite measurements can
45 be supplemented substantially by the long-term ground-based radiation data collected with high temporal resolution at multiple sites with worldwide locations (Remer et al., 2023). For example, Aerosol Robotic Network (AERONET) Program with worldwide distributed sites has provided columnar *AODs* at seven wavelengths (380, 440, 500, 675, 870, 1020, 1640 nm) from the direct-beam irradiance measured by Cimel sunphotometers (CSPHOT; Holben et al., 1998; Giles et al., 2019). Similar to the AERONET sunphotometers, Multi-Filter Rotating Shadowband Radiometers (MFRSRs) supported by the U.S. Department of
50 Energy's (DOE's) Atmospheric Radiation Measurement (ARM) Program (Sisterson et al., 2016; Miller et al., 2016) and the National Oceanic and Atmospheric Administration's (NOAA's) Surface Radiation budget network (SURFRAD; Augustine et al., 2008) have provided *AODs* at five wavelengths (415, 500, 615, 675, 870 nm) for many locations from the direct irradiances. These irradiances have been obtained from the MFRSR-measured total and diffuse solar irradiances. Additionally, the MFRSR data have been used to derive aerosol, cloud, and surface properties (Riihimaki et al., 2021), and to quantify the spectrally
55 resolved radiative impact of clouds (Kassianov et al., 2011). Recently, ARM has added a new channel at 1625 nm wavelength to the ARM-supported MFRSRs.

The limited number of wavelengths coupled with a quite narrow spectral range of the MFRSR prevent improved retrievals of cloud, aerosol, and surface characteristics, and thus preclude advanced understanding of complex cloud-aerosol-surface interactions (Barthlott et al., 2022; Calderón et al., 2022). To address the outlined limitation, ARM developed a hyperspectral
60 shortwave radiometer, called the Shortwave Array Spectroradiometer-Hemispheric (SAS-He), that has collected data since 2011. This ground-based radiometer is a next-generation of the MFRSR with increased spectral coverage (350-1700 nm) and hyperspectral ability. Here we illustrate its performance by taking advantage of an integrated dataset collected by collocated ground-based sensors over coastal regions during three campaigns: (1) Two-Column Aerosol Project (TCAP; Cape Cod, Massachusetts) (Berg et al., 2016), (2) Tracking Aerosol Convection Interactions Experiment (TRACER; in and around



65 Houston, Texas) (Jensen et al., 2022) and (3) Eastern Pacific Cloud Aerosol Precipitation Experiment (EPCAPE; La Jolla,
California) (Russell et al., 2021). The following four sections cover the SAS-He design and calibration procedures (Sect. 2),
a concise description of ground-based data collected during three campaigns (TCAP, TRACER, and EPCAPE) (Sect. 3),
evaluation of the SAS-He *AOD*, total optical depth (*TOD*), direct-to-diffuse ratio (*DDR*), diffuse irradiance (Sect. 4), and a
summary of main results (Sect. 5). It should be emphasized that the spectrally resolved *AODs* offer a valuable avenue for
70 estimating aerosol columnar size distributions (e.g., King et al., 1978; Sayer et al., 2012; Kassianov et al., 2021; Torres and
Fuertes, 2021). Aerosol intensive properties, including single-scattering albedo and asymmetry parameter, are possible through
retrievals combining *AODs* and *DDRs* (e.g., Kassianov et al., 2007; Ge et al., 2010). Additionally, the favorable comparisons
demonstrated in our paper can be considered as foundational for future activities including improved understanding of changes
in photosynthetically active radiation, and refinement of broadband radiation measurements and radiative transfer calculations.
75 Finally, the potential exists to retrieve cloud properties, such as cloud optical depth and droplet effective radius, by examining
wavelength-dependent diffuse irradiance under overcast conditions (e.g., LeBlanc et al., 2015).

2 SAS-He design, calibration and corrections

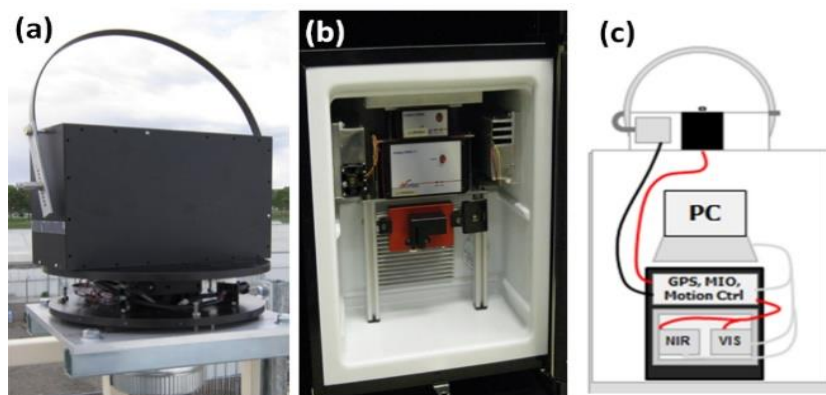
The SAS-He is the successor to the MFRSR (Hodges and Michalsky, 2016) and the Rotating Shadow band Spectroradiometer
80 (RSS; Michalsky and Kiedron, 2022). The SAS-He employs the shadow band technique (Wesely, 1982; Harrison et al., 1994)
and its design, operation and calibration are borrowed heavily from the predecessors. The corresponding detailed reviews are
presented elsewhere (Hodges and Michalsky, 2016; Flynn, 2016; Michalsky and Kiedron, 2022), and here we provide only a
brief description sufficient to acquaint the reader with enhanced capabilities of the SAS-He.

2.1 Design

85 Figure 1 shows the major elements of the SAS-He instrument. The overall design is composed of an optical collector (Fig. 1a)
located outdoors connected to a pair of chilled spectrometers (Fig. 1b) and data collections system located indoors within a
climate-controlled environment (Fig. 1c). Photons incident on the hemispheric diffuser at the fore-optics of the light collector
travel through a large single core optical fiber to a 50/50 bifurcated Y-fiber that diverts the signal to the UV-VIS-NIR and
SWIR spectrometers. Within each spectrometer, the light is spectrally dispersed by a diffraction grating and focused onto a
90 solid-state linear detector array. The array is then read by an electronic interface that passes the data to the computer where it
is stored. The data acquisition electronics and spectrometers include an in-line fiber optic shutter for automatic dark signal
correction. Dark signals are obtained periodically by closing the in-line shutter and collecting spectra with the same integration
time that was used to measure the sky intensity. The thermostatically-controlled ($\pm 1^\circ\text{F}$) refrigerator (Fig.1b) is supplied with
dry air and/or desiccant to prevent condensation. The connection of the sky collection optics, rack-mounted data acquisition
95 equipment and fiber-coupled UV-VIS-NIR and SWIR spectrometers is provided by fiber optic and electrical cables (Fig.1c).



The optical collector, based strongly on the designs of the MFRSR and RSS, includes a hemispheric diffuser and a moving shadow band (Fig. 1a) for distinguishing direct solar and diffuse sky irradiance at approximately 30 sec temporal resolution. A fiber optic umbilical with an in-line shutter connects the optical collector to a pair of commercial off-the-shelf Avantes spectrometers (Fig. 1b) with a wide spectral coverage and high spectral resolution (Table 1). Certainly, this important capability is superior to the MFRSR, since it increases substantially the opportunity to extend the existing MFRSR-based retrievals to expected multidisciplinary studies with focus on the climate-important properties (Riihimaki et al., 2021). For example, unique absorption and scattering properties of ice and liquid water cloud particles can be retrieved from cloud-transmitted radiance spectra measured with a wide spectral coverage and high spectral resolution (e.g., LeBlanc et al., 2015). The main consideration in the design of the SAS-He instrument was to obtain high radiometric repeatability and efficiency. To address this challenge, several modifications of the MFRSR-like configuration have been made. The next sections highlight these valuable modifications.



110 **Figure 1: The SAS-He design: (a) shadow band and sky collection optics mounted outside, (b) UV-VIS-NIR and SWIR spectrometers housed inside the chiller, (c) instrument layout concept.**

Table 1. A pair of SAS-He spectrometers: Main characteristics

Spectrometers	Range	Resolution
UV-VIS-NIR fiber-coupled spectrometer (Avaspec ULS 2048 CCD)	350-1040 nm	~2.4 nm
SWIR fiber-coupled spectrometer (Avaspec NIR256-1.7)	990-1700 nm	~ 6 nm
Angular sampling	Range	Field-of-view
Total and diffuse irradiances	Full hemisphere	~ 3.6 deg (shadowband full-angle)



115 2.2 SAS-He calibrations

Several aspects of the SAS-He require careful characterization and/or calibration. Some of these are commonly applied to legacy solar radiometers, but some are unique to the hyperspectral measurements of the SAS-He. These corrections and calibrations are described briefly below.

2.2.1 Spectral registration

120 The Avantes grating array spectrometers, calibrated in terms of wavelength prior to delivery, include a multi-order polynomial fit providing wavelength as a function of pixel index number. We confirmed the wavelength mapping is accurate to within a pixel by confirming the location of known emission lines from a Mercury-Argon discharge lamp. In addition, reference to sharp Fraunhofer lines (emission and absorption lines in the solar spectrum) in the UV and visible spectra and well-known atmospheric absorption features including water vapor bands and the oxygen A-band permit in-field confirmation of the
125 spectral registration, a practice which is not typically feasible for filter-based measurements.

2.2.2 Spectral resolution

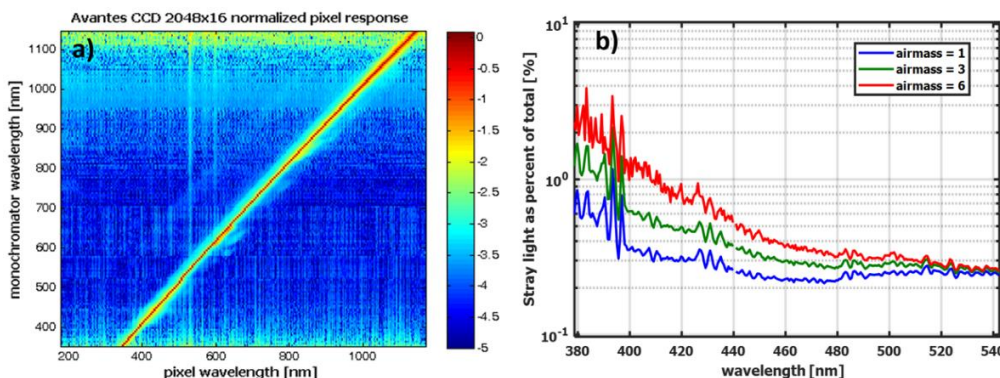
In addition to the pixel-to-wavelength mapping, Avantes also provides the approximate spectral resolution for each spectrometer configuration. For the Si CCD spectrometer, the nominal spectral resolution is about 2.5 nm full width at half maximum (FWHM). The nominal spectral resolution of the InGaAs array spectrometer is about 6 nm FWHM. Note that the
130 spectral resolution is distinct from the pixel spacing which is the wavelength difference between adjacent pixels as inferred from the spectral registration above. The pixel spacing for the Si CCD is about 0.55 nm. The pixel spacing for the InGaAs array is about 3.5 nm. This means that the spectra from the Si CCD is being over-sampled by about a factor of four, while the InGaAs array is being over-sampled by about a factor of two.

2.2.3 Internal stray light within the spectrometer

135 Stray light in the spectrometer, similar to out-of-band leakage for narrow-band filter measurements, represents signal from other wavelengths detected and ascribed to the intended wavelength. We have measured stray light scattered internally within the spectrometer by scanning a double-slit monochromator positioned in front of a broadband light source over the spectral range of the spectrometer. Except for a few isolated “hot pixels,” the stray-light levels are below 0.1 to 0.01% over most of the spectral range as shown in Figure 2a. The horizontal axis is the wavelength reported by the grating spectrometer. The
140 vertical axis is the source wavelength provided by the scanning monochromator. The vivid diagonal line indicates that most light is detected at the spectrometer pixels corresponding to the monochromator selected wavelength. However, some spectrometer artifacts are apparent as wisps about the diagonal line, and a ghostlike diagonal feature offset from the diagonal by about 200 nm. The color scale is log-base 10, so a value of -3 (cyan) is 0.1% intensity of stray light relative to the peak signal intensity. Although initially assumed to represent a negligible contribution, the accumulation of even these low



145 scattering levels generated aberrant behavior at the wavelength limits of the UV/VIS spectrometer that required empirical
correction.



150 **Figure 2:** Panel (a) shows results of a stray light measurement for the SAS-He Si CCD obtained by placing a scanning
monochromator at the entrance port of the Si CCD grating spectrometer. The horizontal axis is the wavelength
reported by the grating spectrometer. The vertical axis is the source wavelength provided by the scanning
monochromator. Panel (b) shows the empirical stray light correction of the SAS-He direct horizontal irradiance as a
proportion of the raw uncorrected signal for three airmass values over the short wavelength range where this correction
is most significant.

155 Figure 2b illustrates that the stray light correction is more significant at shorter wavelengths and depends strongly on airmass.
The result of the stray light is that the Langley calibrations for short wavelengths become skewed and artificially shallow,
leading to low calibration bias and low retrieved *AODs*. The empirical correction shown in Figure 2b yields satisfactory
calibration up to 380 nm.

2.2.4 External stray light detected by the spectrometer

160 There are two potential sources of external light affecting the SAS-He irradiance measurements. The first is direct sunlight
leaking through the fiber-optic jacketing of the umbilical. By exposing and shading the optical collector under direct solar
exposure we have confirmed that leakage, if it exists at all, is at undetectable levels. In addition, since 2019 the in-line shutter
(the red device in Fig. 1b) has been moved out of the chiller and incorporated into the collector head such that fiber leakage
would represent common signal and be subtracted as “dark” counts.

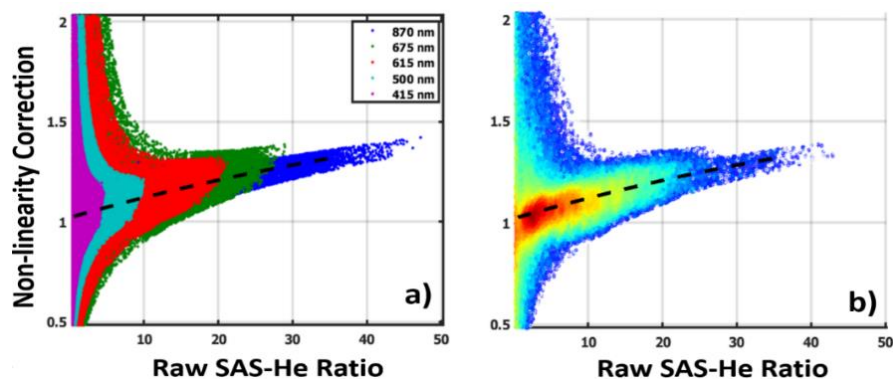
165 The second potential source of stray light is from reflective objects near the collector head producing glint detectable by
the SAS-He in the diffuse hemispheric irradiance measurement. This was observed and documented for the Go-Amazon
deployment (not part of this study) due to the proximity of the SAS-He adjacent to a 10-meter-high stainless-steel aerosol
sampling stack. This unfortunate configuration was avoided for the deployments in this study.

2.2.5 Non-Lambertian response of the optical collector, “cosine correction”

170 Hemispheric collectors used by the MFRSR and the SAS-He exhibit a dependence on the angle of incidence of incoming light.
For an ideal Lambertian diffuser this dependence is exactly the cosine of the incident angle. The angular response of the SAS-
He collector is carefully characterized in lab measurements where the collector is mounted on a rotating stage and exposed to
a stationary light source. The lab-derived “cosine correction” is applied to the direct beam measurements, and a variant of the
cosine correction is also applied to the diffuse field as the average of the modeled response to isotropic, clear-sky, and overcast
175 conditions.

2.2.6 Spectrometer signal non-linearity

Photodiodes used in the MFRSR and CSPHOT instruments have demonstrated excellent signal linearity spanning several
orders of magnitude. In contrast, the SAS-He spectrometers require careful linearity characterization. By varying incident light
levels and integration times, we have documented the non-linearity for each grating spectrometer. The non-linearity is small,
180 though not negligible. To first order, the non-linearity of the direct irradiance measurement becomes incorporated in the cosine
correction described above, but the diffuse hemispheric component requires further correction. To infer this correction, we
apply the following two-step approach. First, we calculate the direct-to-diffuse ratio by dividing the direct-normal irradiance
by diffuse hemispheric irradiance at a given wavelength. We use the direct-normal irradiances and diffuse hemispheric
irradiances measured by two collocated ground-based instruments, namely the SAS-He and MFRSR. It should be emphasized
185 that the calculated SAS-He and MFRSR direct-to-diffuse ratios are calibration-independent in the sense that this is a unitless
ratio. Second, we obtain an empirical non-linearity correction to the SAS-He diffuse hemispheric irradiance by dividing the
calculated SAS-He ratio by its MFRSR counterpart and then applying the second order polynomial fit (Fig. 3). We apply this
correction to the SAS-He diffuse hemispheric irradiance. Its corrected values are used for the corresponding assessment of the
SAS-He products (Sect. 4).



190

Figure 3: Example of non-linearity correction as a function of the SAS-He direct-to-diffuse ratio obtained during the TRACER. (a) Relationship displayed for five MFRSR filter wavelengths (415, 500, 615, 675, 870nm) shows a progression along a common tendency. (b) A density plot of all corrections irrespective of filter wavelength. Dashed lines indicate the polynomial fits (a,b).

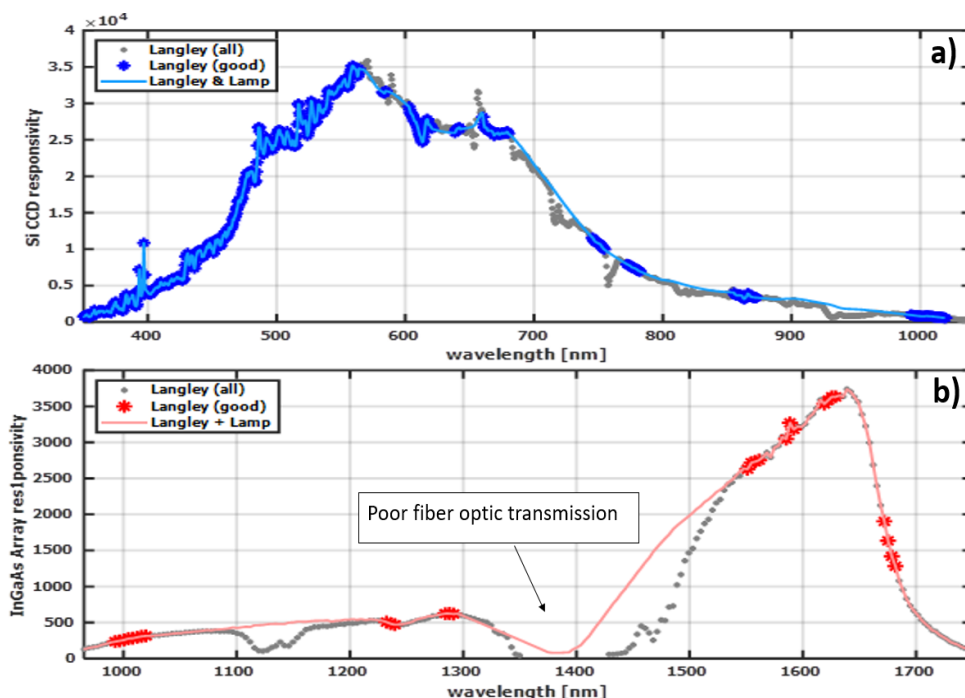


195 2.2.7 Spectrometer signal temperature sensitivity

The CCD spectrometers have been confirmed to exhibit a temperature response of less than 0.1% per degree. The InGaAs spectrometers show higher temperature dependent sensitivity, but this is mostly due to changes in thermal background levels that we address through frequent (~30 sec interval) dark measurements. We have also identified that the InGaAs spectrometers show a trough in their temperature response, so we operate our chiller centered on this minimum in temperature sensitivity.

200 2.2.8 Spectrometer responsivity

A Newport Oriel OPS-Q250 and 200 W QTH lamp with NIST-traceable spectral calibration from 250-2400 nm was used to measure the SAS-He relative spectral response. Based on reproducibility, the absolute uncertainty of the measurement is estimated to be up to several percent, insufficient for independent irradiance calibration. However, comparison of normalized responsivity curves shows relative variation less than 0.1% over the full spectral range after a 10-min lamp settling time. The
205 relative spectral responsivity is scaled to agree with Langley calibration to top-of-atmosphere solar irradiance (Fig. 4) using the conventional approach (Kindel et al., 2001; Michalsky and Kiedron, 2022).

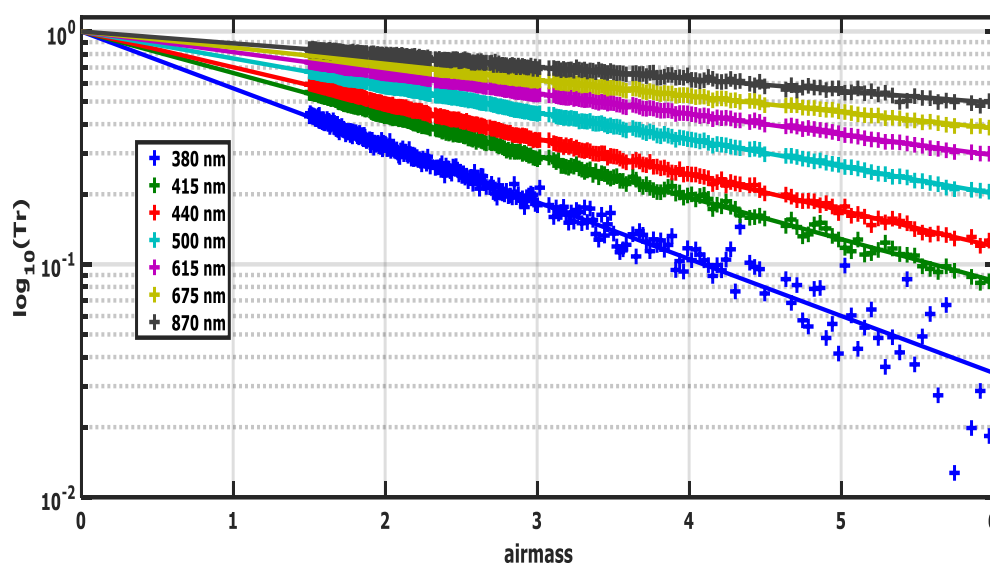


210 **Figure 4: The spectral responsivity of the Si CCD (a) and InGaAs (b) array. In both figures (a,b) the gray dots show the spectral responsivity obtained through dividing the Langley regression Y-intercept by top-of-atmosphere solar irradiance at each wavelength. The colored asterisks represent those wavelengths where Langley regressions are anticipated to be dependable under suitable atmospheric conditions. The fine blue (Si CCD) and pink (InGaAs Array) lines represent the responsivity obtained as a combination of Langley calibration with lamp calibration. These lines are labeled as “Langley + Lamp.”**



215 2.2.9 Langley calibration (direct irradiance)

To determine *AODs* from the SAS-He measurements, in-field calibration with Langley regressions is applied. Recall that the Langley regressions are linear regressions of log of the measured irradiance versus airmass and they are computed on a twice daily basis. The output of these regressions (Fig. 5) is used for field calibration of the SAS-He. Since the daily Langley regressions exhibit significant noise mostly due to atmospheric variability, several weeks of SAS-He operational measurements
220 are required to accumulate enough acceptable Langley regressions with small (below 1% per day) statistical variability. Application of a stable daily calibration to the SAS-He radiometric measurements allows one to calculate time series of *TOD* for each wavelength.



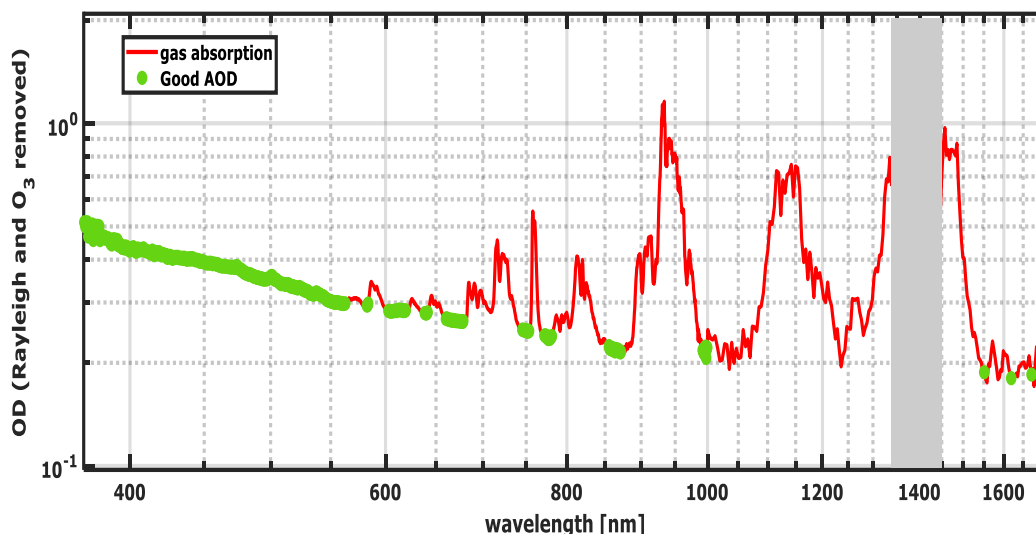
225 **Figure 5:** Example of a SAS-He Langley plot from July 18, 2021 at several CSPHOT and MFRSR wavelengths during TRACER. To demonstrate the expected monotonic behavior with wavelength (with shorter having the steepest slopes and largest optical depths) more clearly, the signal for each wavelength is normalized against the Y-intercept of the Langley regression line forcing each to intersect at 0 airmass.

2.2.10 Total optical depth and gaseous absorption

230 Figure 6 shows an example of the *TOD* spectra obtained from the SAS-He “UV-VIS-NIR” spectrometer. The first “UV/VIS” segment (from about 400 to 450 nm) does not include gaseous absorption. The exception is very small NO_2 absorption, which can be neglected for many practical applications. Thus, the *TOD* spectrum in this spectral range represents sufficiently well the actual *AOD*. The second segment (from about 450 to 750 nm) includes substantial ozone absorption in the Chappuis band. The finding of the ozone optical depth requires an estimate of the columnar amount of ozone. Data from the Total Ozone
235 Mapping Spectrometer (TOMS; <http://toms.gsfc.nasa.gov>) or from the Ozone Monitoring Instrument (OMI;



240 <http://aura.gsfc.nasa.gov/instruments/omi.html>) can be used for obtaining the required ozone amount for a given SAS-He location. We continue with spectra obtained from the SAS-He “SWIR” spectrometer (Fig. 6). The gaseous absorption is quite large for the majority of spectral regions, and thus it precludes the straightforward inference of *AOD* from the measured *TOD* spectrum. There are, however, several spectral areas with minimal gaseous absorption (e.g., segments around 1020 and 1620 nm wavelengths) where the gaseous absorption can be accounted for.



245 **Figure 6: Example of *TOD* spectrum with the Rayleigh component and O₃ removed during the TRACER. The green symbols show approximate spectral regions where the *AOD* may be effectively retrieved. *AODs* may be found across short wavelength segments from about 400 to 675 nm and about 778 and 870 nm. Near-infrared segments suitable for retrieving of *AOD* are centered on 1020 nm and 1623 nm wavelengths, but care must be used to avoid regions of strong gaseous absorption. The SAS-He fiber optics are opaque near 1400 nm thus this region has been greyed out.**

3 ARM-supported campaigns

250 The evaluation of a new instrument requires two main considerations. The first consideration is a wide range of observational conditions associated with different aerosol and cloud types and strong variability of aerosol loading. The second consideration is availability of good-quality data offered by collocated and coincident instruments with different designs and operations. The three ARM Mobile Facility (AMF) campaigns selected for this analysis provide ground-based instruments for measuring aerosol, cloud, precipitation, and atmospheric state properties and satisfy these challenging considerations. The interested reader can find detailed descriptions of these campaigns at www.arm.gov, which are of significant scientific interest, their suites of ground-based instruments, with state-of-the-art capabilities, and the corresponding data (Berg et al., 2016; Jensen et al., 2022; Russell et al., 2021). Here we summarize these campaigns conducted over climatologically important regions and highlight only data used for our evaluation, specifically, the spectrally resolved *AOD*, *TOD*, as well as the diffuse irradiance and *DDR*.



For each campaign, we compare data provided by MFRSR, CSPHOT and SAS-He. The quality assured (level 2) *AODs* measured at seven (380, 440, 500, 675, 870, 1020, 1640 nm) wavelengths by CSPHOT with a sun-pointing design are used as a “reference” for evaluation of SAS-He *AODs* (Sect. 4.1). The spectrally resolved *DDRs* and diffuse irradiances provided by MFRSR are used as a “reference” for evaluation of their SAS-He counterparts (Sect. 4.2, 4.3). Recall, MFRSR and SAS-He are sensors with hemispherical receptors that are periodically shaded by rotating bands. The evaluation involves two groups of the *DDRs* and diffuse irradiances offered by the MFRSR measurements. The first group defines the MFRSR products obtained at the *five available* wavelengths (415, 500, 615, 675, 870 nm) during the TCAP only. The second group defines the MFRSR products obtained at the *six available* wavelengths (415, 500, 615, 675, 870, 1625 nm) during the TRACER and EPCAPE.

3.1 TCAP

The main objective of the TCAP was to examine the evolution of optical and microphysical properties of atmospheric aerosol transported from North America to the Atlantic and their impact on the radiation energy budget (Berg et al., 2016). To achieve this goal, the AMF site (42.03°N; 70.05°W) has been deployed on Cape Cod from July, 2012 through June, 2013. Cape Cod is an arm-shaped peninsula situated on the easternmost portion of Massachusetts, along the U.S. East Coast and is generally downwind of several metropolitan areas. The AMF site was located nearby off-shore Martha’s Vineyard Coastal Observatory (41.30°N, 70.55°W) with CSPHOT (<https://aeronet.gsfc.nasa.gov>).

3.2 TRACER

The main objective of the TRACER was to examine aerosol-cloud interactions in deep convection over the Houston metropolitan area of Texas (Jensen et al., 2022). To achieve this goal, the AMF site (29.67°N; 95.06°W) has been deployed near La Porte, Texas airport from October, 2021 through September, 2022. This area with frequent isolated convective systems is characterized by distinct aerosol types originated, for example, from urban, industrial, and marine sources. The CSPHOT was collocated with the MFRSR and SAS-He as part of the AMF.

3.3 EPCAPE

The main objective of the EPCAPE is to characterize the radiative properties, aerosol interactions, precipitation characteristics, and extent of stratocumulus clouds in the Eastern Pacific across all four seasons (Russell et al., 2021). To achieve this goal, a 12-month deployment of the AMF site (32.87°N; 117.26°W) on Scripps Pier (La Jolla, California) was started on February, 2023. This area with coastal orography and frequently observed transitions from overcast cloud layers to broken clouds is influenced by distinct aerosol types originated from the Los Angeles-Long Beach urban port megacity. The CSPHOT is collocated with the MFRSR and SAS-He as part of the AMF.



4 Evaluation

This section contains comparison of the aerosol-related (both *AOD* and *TOD*) and radiative (both diffuse irradiance and *DDR*) properties provided by the SAS-He with those offered by the collocated ground-based instruments, specifically the MFRSR and CSPHOT, during three selected campaigns highlighted above (Sect. 3). We start with assessment of *AOD* and *TOD* measured at different wavelengths by the SAS-He and CSPHOT (Sect. 4.1). Then, evaluation of spectrally resolved *DDR* offered by the SAS-He and MFRSR is presented (Sect. 4.2). Finally, the diffuse irradiances measured at different wavelengths by the SAS-He and MFRSR are contrasted (Sect. 4.3).

4.1 AOD: SAS-He versus CSPHOT

When a straight line between the Sun and the ground-based instrument is cloud-free, one can calculate *AOD* from *TOD* at a given wavelength (e.g., Giles et al., 2019):

$$AOD(\lambda) = TOD(\lambda) - \tau_{Ray}(\lambda) - \tau_{gas}(\lambda), \quad (1)$$

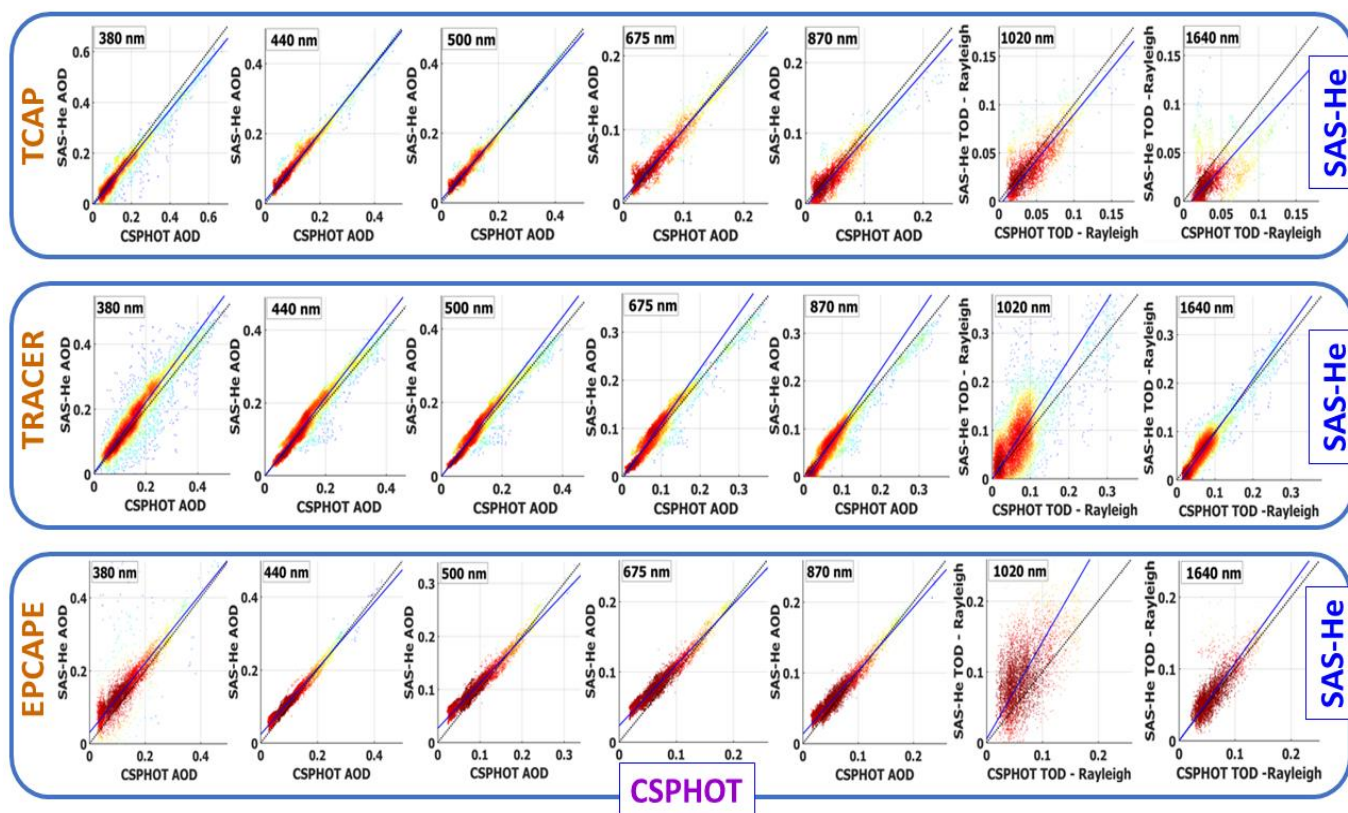
where $\tau_{Ray}(\lambda)$ is Rayleigh optical depth due to molecular scattering and $\tau_{gas}(\lambda)$ is optical depth due to absorption of atmospheric trace gases, such carbon dioxide, methane, and water vapor. The gaseous absorption is relatively small in comparison to *AOD* at five wavelengths (380, 440, 500, 675, 870 nm). In contrast, gas absorption is comparable with *AOD* at other two wavelengths (1020, 1640 nm). Thus, the corresponding corrections of the gas absorption are required for *AOD* calculations at these wavelengths (1020, 1640 nm). The implementation of the required corrections to the SAS-He *AOD* is underway. Here, we compare the available total optical depth adjusted to the Rayleigh scattering, namely $TOD(\lambda) - \tau_{Ray}(\lambda)$, at these wavelengths (1020, 1640 nm). The same $\tau_{Ray}(\lambda)$ is used for such adjustment. The collocated SAS-He and CSPHOT measurements provide the needed *TOD*(λ). Below, both scatterplots (Fig. 7) and the corresponding main statistics (Tables 2-4) illustrate level of agreement between the SAS-He and CSPHOT products (both *AOD* and *TOD*).

Substantial changes of aerosol loading are observed during the TCAP (Fig. 7, top). For example, *AODs* measured by both SAS-He and CSPHOT at 500 nm wavelength can vary over a wide range (roughly from 0.05 to 0.5). The proximity of Cape Cod to the major urban and industrial sources and its frequently downwind location is mainly responsible for the observed substantial changes of aerosol loading. The majority of points are packed around the 1:1 line (Fig. 7, top). The corresponding slopes are close to one (about 0.95), absolute values of intercept are small (about 0.01 or less), and root-mean-square errors (RMSEs) are within the expected measurement uncertainty of *AOD* (0.01-0.02) (Table 2). Both scatterplots and main statistics indicate a strong agreement between SAS-He and CSPHOT *AODs* at the wavelengths considered here. The measurements at longer wavelengths (1020, 1640 nm) show increased scatter (Fig. 7, top) mostly due to reduced signal-to-noise ratio at these wavelengths. For example, mean value of *TOD* measured by CSPHOT at 1640 nm wavelength (0.033) is about three times smaller than the mean value of *AOD* measured by CSPHOT at 500 nm wavelength (0.103). As a result, agreement for *TODs* at longer wavelengths (1020, 1640 nm) is slightly weaker than that for *AODs* at shorter wavelengths (380, 440, 500, 675, 870



nm). To illustrate, the smaller value of slope (0.863) is obtained for *TOD* (SAS-He vs. CSPHOT) at 1640 nm wavelength in comparison with that (0.96) acquired for *AOD* (SAS-He vs. CSPHOT) at 500 nm wavelength (Table 2).

320



325

Figure 7: Density plots of SAS-He *AOD* versus CSPHOT *AOD* measured at five (380, 440, 500, 675, 870 nm; first five columns) wavelengths during the TCAP (top row), TRACER (middle row) and EPCAPE (bottom row), respectively. The corresponding scatterplots of *TOD* adjusted to the Rayleigh scattering at two (1020, 1640nm) wavelengths are also included (last two columns). The short-dashed black line is the 1:1 correspondence line and the solid blue line is the linear regression. Points with light color represent outliers. Note that scales for x- and y-axes depends on wavelength. Tables 2-4 provide the basic statistics of the comparison.

330

Similar to the TCAP, the comparisons during the TRACER and EPCAPE show substantial changes of aerosol loading (Fig. 7). To take an example, *AODs* measured by both SAS-He and CSPHOT at 500 nm wavelength during the TRACER can vary over a wide range (roughly from 0.05 to 0.4) (Fig. 7, middle). In contrast to the TCAP, the TRACER and EPCAPE show slightly different relationships between SAS-He and CSPHOT *AODs* in terms of slope. The slopes calculated for the SAS-He and CSPHOT *AODs* at different wavelengths (380-870 nm) are either larger (1.08-1.18) or smaller (0.85-0.95) than 1.0 for TRACER and EPCAPE, respectively (Tables 3,4). In other words, SAS-He *AODs* tend to be slightly larger than CSPHOT *AODs* during TRACER (Fig. 7, middle). The opposite is true for the EPCAPE (Fig. 7, bottom). The highlighted overestimation and underestimation are likely associated with slightly different SAS-He calibrations performed during the TRACER and

335



EPCAPE. It appears that these trends have only a minor impact on the corresponding RMSEs. The latter are mostly within the expected measurement uncertainty of *AOD* (0.01-0.02) despite these trends (Tables 3,4). Also, comparable RMSEs (0.012-0.013) are obtained for *TOD* at 1640 nm wavelength (Tables 3,4).

340 **Table 2. Parameters of linear regressions (Fig. 7) obtained for CSPHOT and SAS-He *AOD*s measured at seven wavelengths during the TCAP. Root-mean-square error (RMSE) and number of points (N) are also included.**

	380 nm	440 nm	500 nm	675 nm	870 nm	1020 nm	1640 nm
Slope	0.941	0.97	0.96	0.945	0.95	0.948	0.863
Intercept	-0.007	0.008	0.009	0.005	-0.005	-0.005	-0.01
Bias (y-x)	-0.02	0.004	0.004	0.002	-0.007	-0.007	-0.01
Mean (x)	0.144	0.12	0.103	0.064	0.045	0.043	0.033
Mean (y)	0.129	0.124	0.105	0.066	0.038	0.035	0.019
RMSE	0.016	0.008	0.008	0.007	0.01	0.01	0.007
N	4213	4298	4222	4328	4481	4031	3220

Table 3. The same as Table 2 except for the TRACER.

	380 nm	440 nm	500 nm	675 nm	870 nm	1020 nm	1640 nm
Slope	1.08	1.08	1.08	1.15	1.18	1.23	1.12
Intercept	0.004	-0.003	-0.002	-0.006	-0.014	-0.014	-0.016
Bias (y-x)	0.02	0.008	0.007	0.004	-0.003	0.01	-0.008
Mean (x)	0.153	0.127	0.108	0.072	0.059	0.063	0.064
Mean (y)	0.169	0.135	0.115	0.077	0.055	0.077	0.055
RMSE	0.021	0.015	0.013	0.012	0.011	0.034	0.013
N	7804	8503	8435	8219	8058	8152	7954

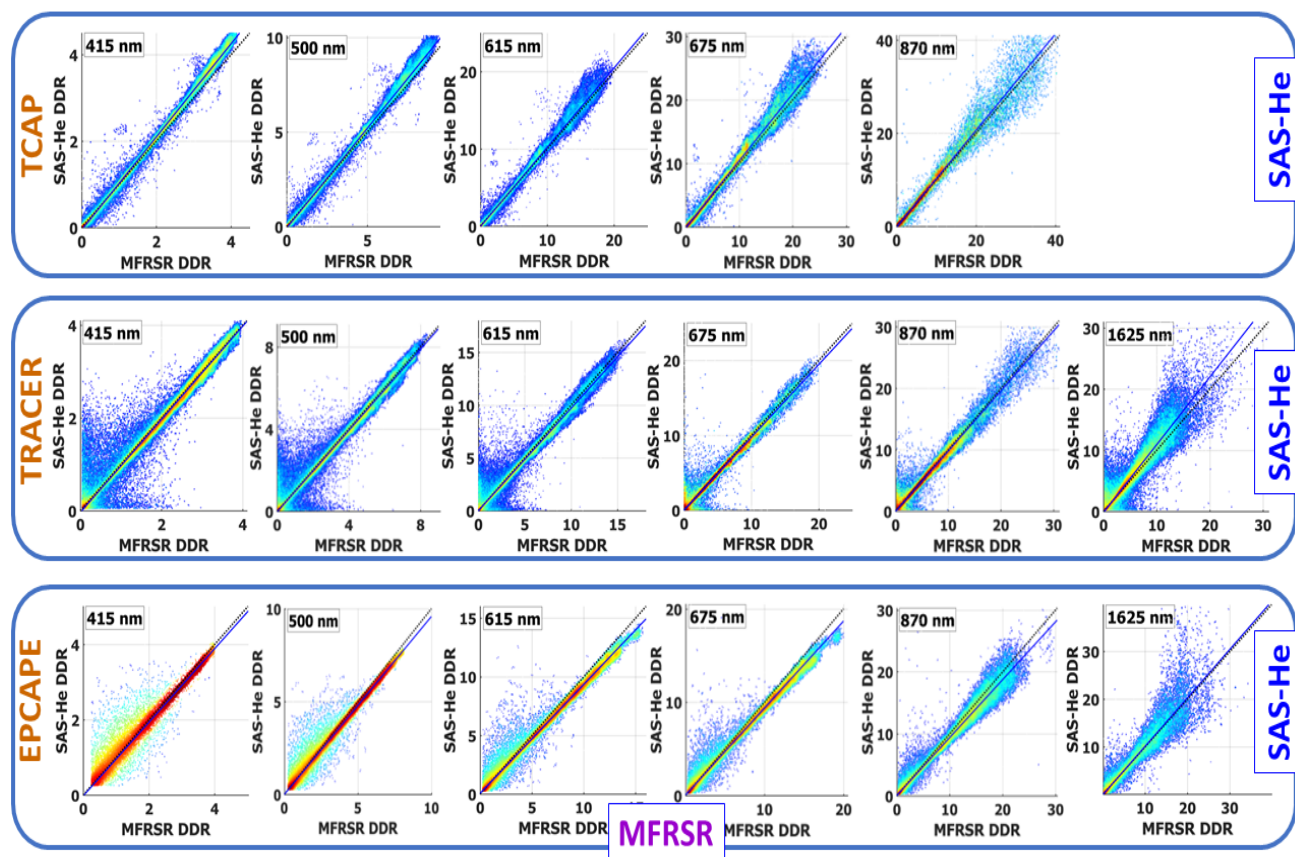
Table 4. The same as Table 2 except for the EPCAPE.

	380 nm	440 nm	500 nm	675 nm	870 nm	1020 nm	1640 nm
Slope	0.95	0.904	0.85	0.867	0.895	1.37	1.08
Intercept	0.03	0.023	0.027	0.023	0.013	0.005	0.0
Bias (y-x)	0.02	0.01	0.01	0.01	0.007	0.03	0.004
Mean (x)	0.116	0.099	0.087	0.068	0.059	0.062	0.057
Mean (y)	0.14	0.113	0.101	0.082	0.066	0.091	0.061
RMSE	0.017	0.01	0.008	0.006	0.007	0.033	0.012
N	7008	7513	7411	7405	7490	4478	4462



345 4.2 DDR: SAS-He versus MFRSR

The *DDR* exhibits even wider range of changes (Fig. 8) than the *AOD* (Fig. 7). These significant changes of *DDR* (about two orders of magnitude) are attributed mainly to two factors. First, the *DDR* comparison (Fig. 8; Tables 5-7) includes both clear- and cloudy-sky conditions where a straight line between the Sun and the ground-based instruments was either cloud-free or blocked by a cloud. Here, the term “cloudy-sky” defines all cloud types observed during the selected campaigns. Typically, different cloud types have distinct and highly variable cloud properties, such as cloud amount and cloud optical thickness, in time and space. Second, the direct and diffuse irradiances vary differently depending on the plume and/or cloud properties. For instance, the *DDR* is small (close to zero; Fig. 8) during the presence of dense plumes associated with strong air pollution emissions or overcast and optically thick clouds. In this case, the direct irradiance is negligible in comparison with the diffuse irradiance. During clean and clear-sky conditions, the direct irradiance reaches large values, while the diffuse irradiance drops off. These conditions are characterized by large *DDRs* (Fig. 8).



360 **Figure 8:** Density plots of *SAS-He DDR* versus *MFRSR DDR* obtained from the direct and diffuse irradiances measured at five (415, 500, 615, 675, 870 nm) wavelengths during the TCAP (top row), and at six (415, 500, 615, 675, 870, 1625 nm) wavelengths during the TRACER (middle row) and EPCAPE (bottom row), respectively. Note that the *DDR* is dimensionless.



Table 5. Parameters of linear regressions (Fig. 8) obtained at five (415, 500, 615, 675, 870nm) wavelengths for MFRSR and SAS-He *DDRs* during the TCAP. Root-mean-square error (RMSE) and number of points (N) are also included.

	415 nm	500 nm	615 nm	675 nm	870 nm
Slope	1.08	1.05	1.03	1.05	1.04
Intercept	-0.058	-0.079	-0.067	-0.1	-0.12
Bias (y-x)	0.09	0.1	0.05	0.2	0.07
Mean (x)	1.88	3.28	4.1	4.88	5.06
Mean (y)	1.97	3.37	4.15	5.03	5.12
RMSE	0.06	0.109	0.126	0.172	0.209
N	62829	57178	40538	37489	29199

365 **Table 6. Parameters of linear regressions (Fig. 8) obtained at six (415, 500, 615, 675, 870, 1625nm) wavelengths for MFRSR and SAS-He *DDRs* during the TRACER. Root-mean-square error (RMSE) and number of points (N) are also included.**

	415 nm	500 nm	615 nm	675 nm	870 nm	1625 nm
Slope	1.0	0.99	0.972	0.973	0.98	1.11
Intercept	-0.039	-0.035	-0.003	0.001	-0.027	-0.18
Bias (y-x)	-0.03	-0.07	-0.1	-0.1	-0.1	0.3
Mean (x)	2.01	3.26	4.44	4.92	5.76	4.81
Mean (y)	1.98	3.19	4.32	4.79	5.62	5.16
RMSE	0.072	0.119	0.18	0.208	0.29	0.52
N	106443	102537	96660	94278	78564	61001

Table 7. The same as Table 6 except for the ECAPE.

	415 nm	500 nm	615 nm	675 nm	870 nm	1625 nm
Slope	0.979	0.958	0.93	0.931	0.935	1.02
Intercept	-0.027	-0.004	0.057	0.063	0.049	-0.048
Bias (y-x)	-0.08	-0.2	-0.4	-0.5	-0.5	0.04
Mean (x)	2.44	4.27	6.51	7.43	8.5	5.08
Mean (y)	2.36	4.08	6.11	6.98	7.99	5.12
RMSE	0.044	0.079	0.178	0.231	0.466	0.513
N	36308	35993	37455	36588	32087	14765



370

A moderate scattering of points with well-defined clustering along 1:1 correspondence line (Fig. 8) indicates that the SAS-He measurements offer the spectrally resolved *DDR* in a reasonable manner. Visually, the scattering of points has campaign-dependent features (Fig. 8). To illustrate, a noticeable number of points are located along the x- and y-axis during the TRACER (Fig. 8, middle). Alternatively stated, the *DDRs* offered by two instruments, namely the SAS-He and MFRSR, occasionally
375 can be quite different when the *DDR* values are small-to-moderate (less than 3). Combination of several potential reasons, such as cloud-induced variability of both the direct and diffuse irradiances at small scales, a minor temporal mismatch due to different reporting times, and the spatial separation of these neighboring instruments (~120 m), could be responsible for different observational conditions for the two instruments (sunlit vs. shadow cases for two instruments spaced slightly apart), and thus could contribute to the highlighted differences. It appears that the level of agreement between the SAS-He *DDR* and
380 MFRSR *DDR* (Tables 5-7) is scarcely affected by the campaign-dependent variability of cloud and aerosol properties: the slope is close to one (0.93-1.1), the mean values are comparable, and these values exceed the RMSE substantially (about ten times or more).

4.3 Diffuse irradiance: SAS-He versus MFRSR

Scatterplots generated for the diffuse irradiances measured by the SAS-He and MFRSR illustrate clearly that these irradiances,
385 on average, are in a good agreement (Fig. 9). It should be emphasized that the diffuse irradiances rely on the calibration. Thus, potential calibration-related issues could have a profound impact on the statistical relationship between these irradiances. The MFRSR lamp calibration issue at 1625 nm wavelength is documented for the ECAPE, and this issue is responsible for the significant disagreement between the diffuse irradiances measured by the SAS-He and MFRSR at 1625 nm wavelength (Fig. 9; bottom). The corresponding slope is very small (0.075) and the difference between mean values of the diffuse irradiances is
390 enormous (0.942 vs. 0.066) (Tables 8-10). It is also vital to note that the accompanying *DDRs* offered by the SAS-He and MFRSR at 1625 nm wavelength are in very good agreement (Fig. 8; bottom), because the *DDRs*, in contrast to the diffuse irradiances, do not depend on calibration. Similar to the *DDR*-related scatterplots (Fig. 8), the scatterplots generated for the diffuse irradiances (Fig. 9) display the campaign-dependent features of points scattering around the 1:1 correspondence line. For example, the TRACER in comparison with the ECAPE has a wider spread of points (Fig. 9, middle vs. bottom). The
395 fraction of points contributing to this spread is small relative to the fraction of points clustering around the 1:1 correspondence line (Fig. 9, middle vs. bottom). Thus, the level of agreement between the main statistics (Tables 8-10) depends slightly on these spread-contributed points.

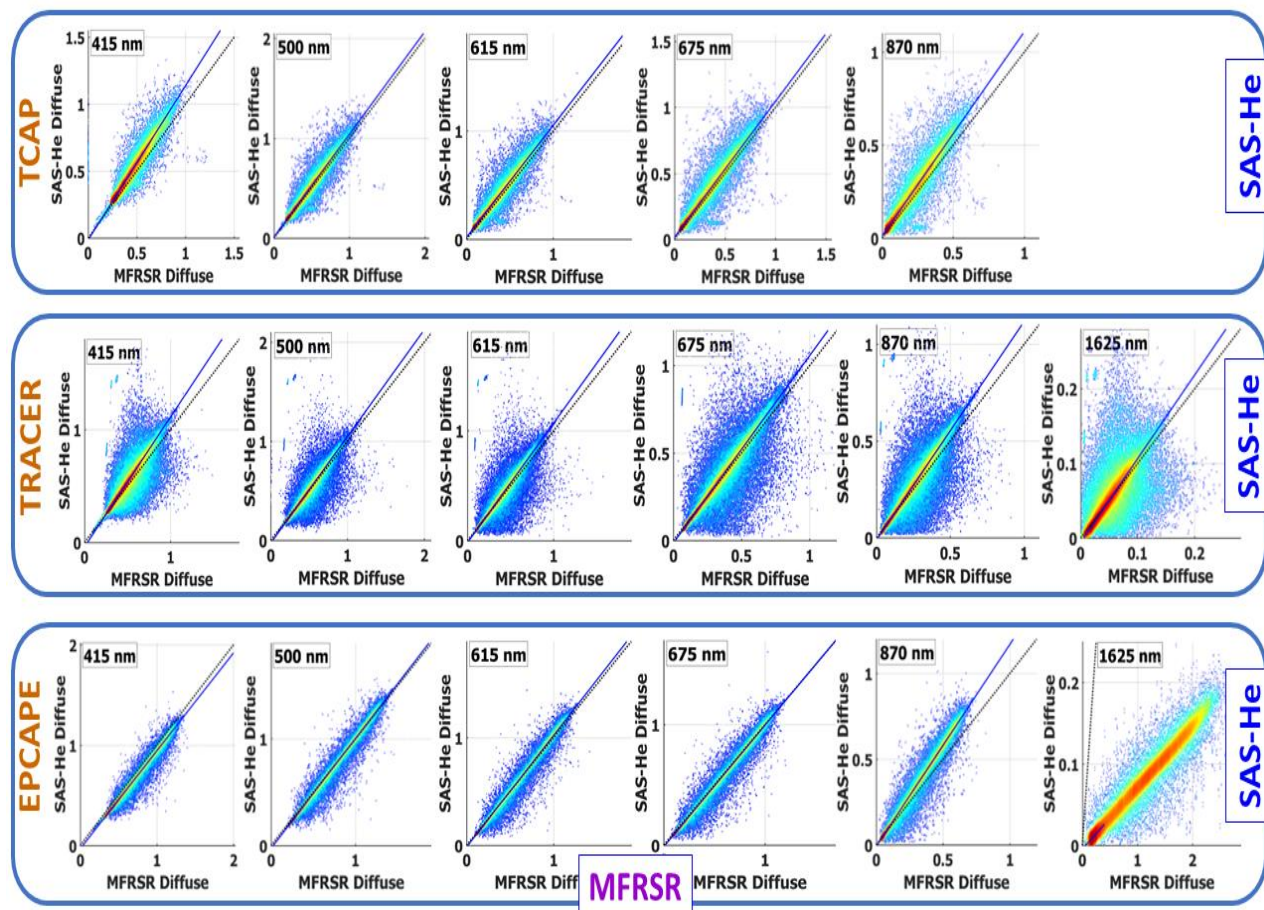


Figure 9: The same as Figure 8 except for the diffuse irradiance ($\text{Wm}^{-2}\mu\text{m}^{-1}$).

400



Table 8. The same as Table 5 except for the diffuse irradiance ($\text{Wm}^{-2}\mu\text{m}^{-1}$).

	415 nm	500 nm	615 nm	675 nm	870 nm
Slope	1.15	1.03	1.03	1.03	1.1
Intercept	-0.016	0.011	0.019	0.017	0.012
Bias (y-x)	0.04	0.02	0.03	0.02	0.02
Mean (x)	0.393	0.34	0.221	0.186	0.113
Mean (y)	0.438	0.361	0.247	0.208	0.136
RMSE	0.014	0.009	0.008	0.008	0.008
N	62252	55624	55053	54895	58773

Table 9. The same as Table 6 except for the diffuse irradiance ($\text{Wm}^{-2}\mu\text{m}^{-1}$).

	415 nm	500 nm	615 nm	675 nm	870 nm	1625 nm
Slope	1.15	1.08	1.09	1.07	1.13	1.12
Intercept	-0.04	-0.029	-0.019	-0.016	-0.012	-0.006
Bias (y-x)	0.02	0.001	0.005	0.002	0.009	-0.001
Mean (x)	0.429	0.389	0.282	0.244	0.165	0.041
Mean (y)	0.453	0.39	0.287	0.246	0.175	0.042
RMSE	0.014	0.013	0.011	0.01	0.009	0.004
N	122849	115156	112052	111491	116957	104351

405 **Table 10. The same as Table 7 except for the diffuse irradiance ($\text{Wm}^{-2}\mu\text{m}^{-1}$).**

	415 nm	500 nm	615 nm	675 nm	870 nm	1625 nm
Slope	0.975	1.03	1.04	1.01	1.18	0.075
Intercept	-0.033	-0.028	-0.016	-0.014	-0.01	-0.005
Bias (y-x)	-0.05	-0.01	-0.002	-0.01	0.03	-0.9
Mean (x)	0.598	0.525	0.394	0.355	0.218	0.942
Mean (y)	0.551	0.514	0.392	0.344	0.247	0.066
RMSE	0.008	0.008	0.006	0.005	0.006	0.004
N	54988	51920	49595	49338	54685	45482



5 Summary

410 We introduce a ground-based radiometer, the so-called Shortwave Array Spectroradiometer-Hemispheric (SAS-He), with an
increased spectral coverage (350-1700 nm) and improved spectral resolution. The latter is about 2.4 nm and 6 nm in the UV-
VIS-NIR (350-1040 nm) and SWIR (990-1700 nm) spectral ranges, respectively. The SAS-He measures the spectrally resolved
total irradiance and its direct and diffuse components with high temporal (30 sec) resolution. Both aerosol optical depth (*AOD*)
and total optical depth (*TOD*) are derived from the direct irradiance measured by the SAS-He, while direct-to-diffuse ratio
415 (*DDR*) is calculated using two components of the measured total irradiance. We assess performance of the SAS-He using
integrated datasets collected during three field campaigns supported by the U.S. Department of Energy's (DOE's) Atmospheric
Radiation Measurement (ARM) Program: (1) Two-Column Aerosol Project (TCAP) (Berg et al., 2016), (2) Tracking Aerosol
Convection Interactions Experiment (TRACER) (Jensen et al., 2022), and (3) Eastern Pacific Cloud Aerosol Precipitation
Experiment (EPCAPE) (Russell et al., 2021). These campaigns represent climatologically important regions with different
420 types of aerosols originated from the major marine, urban and industrial sources.

For our assessment we use data offered by three collocated ground-based instruments, namely Multi-Filter Rotating
Shadowband Radiometer (MFRSR), Cimel sunphotometer (CSPHOT) and SAS-He, as part of the ARM Mobile Facility
(AMF). Our assessment involves (i) *AOD* measured at five (380, 440, 500, 675, 870 nm) wavelengths and *TOD* measured at
two wavelengths (1020 and 1640 nm) by the SAS-He and CSPHOT, (ii) the diffuse irradiance and *DDR* provided by the SAS-
425 He and MFRSR at five (415, 500, 615, 675, 870 nm) wavelengths during the TCAP, and (iii) the diffuse irradiance and
DDR provided by the SAS-He and MFRSR at six (415, 500, 615, 675, 870, 1625 nm) wavelengths during the TRACER and
EPCAPE. The measurements of the diffuse irradiance and *DDR* define all-sky observational conditions when a straight line
between the Sun and the ground-based instruments was either cloud-free or blocked by a cloud. Data provided by the CSPHOT
and MFRSR are considered as “reference” during our assessment.

430 We compare the spectrally resolved parameters related to aerosol loading (both *AOD* and *TOD*) and radiative properties
(both diffuse irradiance and *DDR*) supplied by the SAS-He with those provided by the CSPHOT and MFRSR using scatterplots
and the main statistics, such as slope and intercept of linear regression, and root-mean-square error (RMSE). Our comparison
demonstrates that, on average, the SAS-He properties match closely their MFRSR and CSPHOT counterparts despite the
challenging observational conditions associated with large variability of aerosol loading and distinct types of aerosols and
435 clouds. In particular, the *AOD*- and *TOD*-related RMSEs are within the expected measurement uncertainty of *AOD* (0.01-0.02)
for the majority of cases. Moreover, the slope is mostly close to one (0.85-1.18) and absolute values of intercept are mostly
near zero (less than 0.07) for both the aerosol and radiative properties considered here. It is expected that SAS-He data collected
for a period exceeding 10 years (since 2011) will be used to derive previously unavailable or enhanced data products of aerosol,
clouds, surface (e.g., Riihimaki et al., 2021) at multiple sites with worldwide locations and these ground-based products
440 combined with those offered by aircraft and satellite observations (Remer et al., 2023) will be imperative in the context of
evaluation and improvements of model predictions.



Data availability

Data can be downloaded from the ARM data archive (<https://www.arm.gov/data/>).

CSPHOT: <http://dx.doi.org/10.5439/1461660>

445 MFRSR: <http://dx.doi.org/10.5439/1356805>

MFRSR7nch: <http://dx.doi.org/10.5439/1756632>

SAS-He vis: <http://dx.doi.org/10.5439/1110768>

SAS-He nir: <http://dx.doi.org/10.5439/1110710>

Author contribution

450 Conceptualization, E.K. and C.J.F. with input from J.C.B. Data processing, B.D.E. Formal Analysis, E.K. and C.J.F. Writing – Original Draft, E.K.; Writing-Review & Editing, E.K. and C.J.F. with input from J.M.C.

Competing interest

The author declare that they have no conflict of interest.

Acknowledgements

455 This research was supported by the U.S. Department of Energy (DOE), Office of Science Biological and Environmental Research, as part of the Atmospheric Radiation Measurement (ARM) user facility. The Pacific Northwest National Laboratory is operated for DOE by the Battelle Memorial Institute under Contract DEAC05-76RL.

References

- 460 Augustine, J.A., Hodges, G.B., Dutton, E.G., Michalsky, J.J., and Cornwall, C.R.: An aerosol optical depth climatology for NOAA's national surface radiation budget network (SURFRAD), *J. Geophys. Res.*, 113, D11204, 2008.
- Barthlott, C., Zarbo, A., Matsunobu, T., and Keil, C.: Impacts of combined microphysical and land-surface uncertainties on convective clouds and precipitation in different weather regimes, *Atmos. Chem. Phys.*, 22, 10841–10860, <https://doi.org/10.5194/acp-22-10841-2022>, 2022.
- 465 Berg, L.K., Fast, J.D., Barnard, J.C., Burton, S.P., Cairns, B., Chand, D., Comstock, J.M., Dunagan, S., Ferrare, R.A., Flynn, C.J., Hair, J.W., Hostetler, C.A., Hubbe, J., Johnson, R., Kassianov, E.I., Kluzek, C.D., Mei, F., Miller, M.A., Michalsky, J., Ortega, I., Pekour, M., Rogers, R.R., Russell, P.B., Redemann, J., Sedlacek III, A. J., Segal-Rosenheimer, M., Schmid, B., Shilling, J.E., Shinozuka, Y., Springston, S. R., Tomlinson, J., Tyrrell, M., Wilson, J. M., Volkamer, R., Zelenyuk, A., and Berkowitz, C.M.: The Two-Column Aerosol Project: Phase I overview and impact of elevated aerosol layers on aerosol optical depth, *J. Geophys. Res.*, 121, 336–361, <https://doi.org/10.1002/2015JD023848>, 2016.
- 470 Calderón, S. M., Tonttila, J., Buchholz, A., Joutsensaari, J., Komppula, M., Leskinen, A., Hao, L., Moisseev, D., Pullinen, I., Tiitta, P., Xu, J., Virtanen, A., Kokkola, H., and Romakkaniemi, S.: Aerosol–stratocumulus interactions: towards a better process understanding using closures between observations and large eddy simulations, *Atmos. Chem. Phys.*, 22, 12417–12441, <https://doi.org/10.5194/acp-22-12417-2022>, 2022.
- 475 Chen, C., Dubovik, O., Schuster, G.L., Chin, M., Henze, D.K., Lapyonok, T., Li, Z., Derimian, Y., and Zhang, Y.: Multi-angular polarimetric remote sensing to pinpoint global aerosol absorption and direct radiative forcing, *Nat. Commun.*, 13, 7459, <https://doi.org/10.1038/s41467-022-35147-y>, 2022.
- 480 Cochrane, S.P., Schmidt, K.S., Chen, H., Pilewskie, P., Kittelman, S., Redemann, J., LeBlanc, S., Pistone, K., Segal Rozenhaimer, M., Kacenelenbogen, M., Shinozuka, Y., Flynn, C., Ferrare, R., Burton, S., Hostetler, C., Mallet, M., and Zuidema, P.: Biomass burning aerosol heating rates from the ORACLES (ObseRvations of Aerosols above CLouds and their intERactionS) 2016 and 2017 experiments, *Atmos. Meas. Tech.*, 15, 61–77, <https://doi.org/10.5194/amt-15-61-2022>, 2022.



- Coddington, O., Schmidt, K.S., Pilewskie, P., Gore, W.J., Bergstrom, R.W., Roma'n, M., Redemann, J., Russell, P.B., Liu, J., and Schaaf, C.C.: Aircraft measurements of spectral surface albedo and its consistency with ground-based and space-borne observations, *J. Geophys. Res.*, 113, D17209, doi:10.1029/2008JD010089, 2008.
- 485 Flynn, C. J.: Shortwave Array Spectroradiometer–Hemispheric (SASHe) Instrument Handbook. Ed. by Robert Stafford, DOE ARM Climate Research Facility. DOE/SC-ARM-TR-172. <https://doi.org/10.2172/1251414>. 2016, 2016.
- Ge, J.M., Su, J., Ackerman, T.P., Fu, Q., Huang, J.P., and Shi, J.S. : Dust aerosol optical properties retrieval and radiative forcing over Northwestern China during the 2008 China-US joint field experiment, *J. Geophys. Res.*, 115, D00K12, <https://doi.org/10.1029/2009JD013263>, 2010.
- 490 Giles, D.M., Sinyuk, A., Sorokin, M.G., Schafer, J.S., Smirnov, A., Slutsker, I., Eck, T.F., Holben, B.N., Lewis, J.R., Campbell, J.R., Welton, E.J., Korkin, S.V., and Lyapustin, A.I.: Advancements in the Aerosol Robotic Network (AERONET) Version 3 database – automated near-real-time quality control algorithm with improved cloud screening for Sun photometer aerosol optical depth (AOD) measurements, *Atmos. Meas. Tech.*, 12, 169–209, <https://doi.org/10.5194/amt-12-169-2019>, 2019.
- 495 Gumber, A., Reid, J.S., Holz, R. E., Eck, T.F., Hsu, N.C., Levy, R.C., Zhang, J., and Veglio, P.: Assessment of severe aerosol events from NASA MODIS and VIIRS aerosol products for data assimilation and climate continuity, *Atmos. Meas. Tech.*, 16, 2547–2573, <https://doi.org/10.5194/amt-16-2547-2023>, 2023.
- Hansen, J.E. and Travis, L.D.: Light scattering in planetary atmospheres, *Space Sci. Rev.*, 16, 527–610, 1974.
- Harrison, L., Joseph Michalsky, J., and Berndt, J.: Automated multifilter rotating shadow-band radiometer: an instrument for optical depth and radiation measurements, *Appl. Opt.*, 33, 5118–5125, 1994.
- 500 Hodges, G.B. and Michalsky, J.J.: Multifilter Rotating Shadowband Radiometer Instrument Handbook with subsections for derivative instruments: Multifilter Radiometer (MFR) Normal Incidence Multifilter Radiometer (NIMFR). Preprint at https://www.arm.gov/publications/tech_reports/handbooks/mfrsr_handbook.pdf, 2016.
- Holben, B.N., Eck, T.F., Slutsker, I., Tanre, D., Buis, J.P., Setzer, A., Vermote, E., Reagan, J.A., Kaufman, Y., Nakajima, T., 505 Lavenue, F., Jankowiak, I., and Smirnov, A.: AERONET – A federated instrument network and data archive for aerosol characterization, *Remote Sens. Environ.*, 66, 1–16, [https://doi.org/10.1016/S0034-4257\(98\)00031-5](https://doi.org/10.1016/S0034-4257(98)00031-5), 1998.
- Jensen, M.P., Flynn, J.H., Judd, L.M., Kollias, P., Kuang, C., Mcfarquhar, G., Nadkarni, R., Powers, H., Sullivan, J.: A succession of cloud, precipitation, aerosol, and air quality field experiments in the coastal urban environment, *B. Am. Meteorol. Soc.*, 103(2), 103–105. <https://doi.org/10.1175/bams-d-21-0104.1>, 2022.
- 510 Kassianov, E., Flynn, C. J., Ackerman, T. P., and Barnard, J. C.: Aerosol single-scattering albedo and asymmetry parameter from MFRSR observations during the ARM Aerosol IOP 2003, *Atmos. Chem. Phys.*, 7, 3341–3351, <https://doi.org/10.5194/acp-7-3341-2007>, 2007.
- Kassianov, E., Pekour, M., Barnard, J., Flynn, C.J., Mei, F., and Berg, L.K.: Estimation of aerosol columnar size distribution from spectral extinction data in coastal and maritime environment, *Atmosphere*, 12, 1412, <https://doi.org/10.3390/atmos12111412>, 2021.
- 515 Kassianov, E., Barnard, J., Berg, L.K., Long, C.N., and Flynn, C.: Shortwave spectral radiative forcing of cumulus clouds from surface observations, *Geophys. Res. Lett.*, 38, L07801, <https://doi.org/10.1029/2010GL046282>, 2011.
- Kindel, B.C., Pilewskie, P., Schmidt, K.S., Coddington, O., and King, M.D.: Solar spectral absorption by marine stratus clouds: Measurements and modeling, *J. Geophys. Res.*, 116, D10203, doi:10.1029/2010JD015071, 2011.
- 520 Kindel, B.C., Qu Z., and Goetz A.F.: Direct solar spectral irradiance and transmittance measurements from 350 to 2500 nm, *Appl. Opt.*, 40(21), 3483–3494, doi: 10.1364/ao.40.003483, 2001.
- King, M.D., Byrne, D.M., Herman, B.M., and Reagan, J.A.: Aerosol size distributions obtained by inversions of spectral optical depth measurements, *J. Atmos. Sci.*, 35, 2153–2167, 1978.
- Kokhanovsky, A.A.: Optical properties of terrestrial clouds, *Earth Sci. Rev.*, 64, 189–241, 2004.
- 525 LeBlanc, S. E., Pilewskie, P., Schmidt, K. S., and Coddington O.: A spectral method for discriminating thermodynamic phase and retrieving cloud optical thickness and effective radius using transmitted solar radiance spectra, *Atmos. Meas. Tech.*, 8, 1361–1383, <https://doi.org/10.5194/amt-8-1361-2015>, 2015.
- LeBlanc, S.E., Redemann, J., Flynn, C., Pistone, K., Kacenenbogen, M., Segal-Rosenheimer, M., Shinozuka, Y., Dunagan, S., Dahlgren, R. P., Meyer, K., Podolske, J., Howell, S. G., Freitag, S., Small-Griswold, J., Holben, B., Diamond, M., 530 Wood, R., Formenti, P., Piketh, S., Maggs-Kölling, G., Gerber, M., and Namwoonde, A.: Above-cloud aerosol optical



- depth from airborne observations in the southeast Atlantic, *Atmos. Chem. Phys.*, 20, 1565–1590, <https://doi.org/10.5194/acp-20-1565-2020>, 2020.
- Li, J., Carlson, B.E., Yung, Y.L., Lv, D., Hansen, J., Penner, J.E., Liao, H., Ramaswamy, V., Kahn, R.A., Zhang, P., Dubovik, O., Ding, A., Lacis, A.A., Zhang, L., and Dong, Y.: Scattering and absorbing aerosols in the climate system, *Nat. Rev. Earth Environ.*, 3, 363–379, <https://doi.org/10.1038/s43017-022-00296-7>, 2022.
- 535 Matar, C., Cornet, C., Parol, F., C.-Labonnote, L., Auriol, F., and Nicolas, M.: Liquid cloud optical property retrieval and associated uncertainties using multi-angular and bispectral measurements of the airborne radiometer OSIRIS, *Atmos. Meas. Tech.*, 16, 3221–3243, <https://doi.org/10.5194/amt-16-3221-2023>, 2023.
- Michalsky, J.J. and Kiedron, P.W.: Moderate spectral resolution solar irradiance measurements, aerosol optical depth, and solar transmission, from 360 to 1070 nm, using the refurbished rotating shadow band spectroradiometer (RSS), *Atmos. Meas. Tech.*, 15, 353–364, <https://doi.org/10.5194/amt-15-353-2022>, 2022.
- 540 Miller, M.A., Nitschke, K., Ackerman, T.P., Ferrell, W., Hickmon, N., Ivey, M.: The Atmospheric Radiation Measurement Mobile Facility, The Atmospheric Radiation Measurement (ARM) Program: AMS Monograph, The first 20 years of ARM, *Am. Meteorol. Soc.*, doi:10.1175/AMSMONOGRAPHS-D-15-0051.1, 2016.
- 545 Platnick, S., Meyer, K.G., King, M.D., Wind, G., Amarasinghe, N., Marchant, B., Arnold, G.T., Zhang, Z., Hubanks, P.A., Holz, R.E., Yang, P., Ridgway, W.L., and Riedi, J.: The MODIS cloud optical and microphysical products: Collection 6 updates and examples from Terra and Aqua, *IEEE Transactions on Geoscience and Remote Sensing*, 55(1), 502–525, 10.1109/tgrs.2016.2610522, 2017.
- Puthukkudy, A., Martins, J.V., Remer, L.A., Xu, X., Dubovik, O., Litvinov, P., McBride, B., Burton, S., and Barbosa, H. M. J.: Retrieval of aerosol properties from Airborne Hyper-Angular Rainbow Polarimeter (AirHARP) observations during ACEPOL 2017, *Atmos. Meas. Tech.*, 13, 5207–5236, <https://doi.org/10.5194/amt-13-5207-2020>, 2020.
- 550 Remer, L.A., Levy, R.C., and Martins, J.V.: Opinion: Aerosol remote sensing over the next twenty years, *EGUsphere* [preprint], <https://doi.org/10.5194/egusphere-2023-1221>, 2023.
- Riihimaki, L.D., Flynn, C., McComiskey, A., Lubin, D., Blanchard, Y., Chiu, J.C., Feingold, G., Feldman, D.R., Gristey, J.J., Herrera, C., Hodges, H., Kassianov, E., LeBlanc, S.E., Marshak, A., Michalsky, J.J., Pilewskie, P., Schmidt, S., Scott, R.C., Shea, Y., Thome, K., Wagener, R., and Wielicki, B.: The shortwave spectral radiometer for atmospheric science: Capabilities and applications from the ARM user facility, *B. Am. Meteorol. Soc.*, 102(3), E539–E554, <https://doi.org/10.1175/BAMS-D-19-0227.1>, 2021.
- 555 Russell, L.M., Lubin, D., Silber, I., Eloranta, E., Muelmenstaedt, J., Aiken, A., Wang, D., Petters, M., Miller, M., Ackerman, A., Fridlind, A., Witte, M., Lebsack, M., Painemal, D., Chang, R., Liggio, J., and Wheeler, M.: Eastern Pacific Cloud Aerosol Precipitation Experiment (EPCAPE) Science Plan. DOE/SC-ARM-21-009. U.S. Department of Energy, Office of Science, Office of Biological and Environmental Research, doi:10.2172/1804710, 2021.
- Sayer, A.M., Smirnov, A., Hsu, N.C., Munchak, L.A., and Holben, B.N.: Estimating marine aerosol particle volume and number from Maritime Aerosol Network data, *Atmos. Chem. Phys.*, 12, 8889–8909, <https://doi.org/10.5194/acp-12-8889-2012>, 2012.
- 565 Sisterson, D.L., Pepler, R.A., Cress, T.S., Lamb, P.J., and Turner, D.D.: In The Atmospheric Radiation Measurement (ARM) Program: The First 20 Years. The ARM Southern Great Plains (SGP) site, *Amer. Meteor. Soc.* 57, 6.1–6.14, 2016.
- Torres, B., and Fuertes, D.: Characterization of aerosol size properties from measurements of spectral optical depth: A global validation of the GRASP-AOD code using long-term AERONET data, *Atmos. Meas. Tech.*, 14, 4471–4506, 2021.
- 570 Voigt, A., Albern, N., Ceppi, P., Grise, K., Li, Y., and Medeiros, B.: Clouds, radiation, and atmospheric circulation in the present-day climate and under climate change, *WIREs Clim. Change*, 12, e694, <https://doi.org/10.1002/wcc.694>, 2021.
- Wesely, M., Simplified techniques to study components of solar radiation under haze and clouds, *J. Appl. Meteorol.*, 21, 373–383, 1982.
- 575 Yang, P., Bi, L., Baum, B.A., Liou, K.-N., Kattawar, G.W., Mishchenko, M.I., and Cole, B.: Spectrally consistent scattering, absorption, and polarization properties of atmospheric ice crystals at wavelengths from 0.2 to 100 μm , *J. Atmos. Sci.*, 70, 330–347, doi:10.1175/JAS-D-12-039.1, 2013.